Research article

Ahmed Mekawy and Andrea Alù*

Giant midinfrared nonlinearity based on multiple quantum well polaritonic metasurfaces

https://doi.org/10.1515/nanoph-2020-0408
Received July 20, 2020; accepted August 25, 2020; published online September 14, 2020

Abstract: Ultrathin engineered metasurfaces loaded with multiple quantum wells (MQWs) form a highly efficient platform for nonlinear optics. Here we discuss different approaches to realize mid infrared metasurfaces with localized second-harmonic generation based on optimal metasurface designs integrating engineered MQWs. We first explore the combination of surface lattice resonances and localized electromagnetic resonances in nanoresonators to achieve very large field concentrations. However, when we consider finite size effects, the field enhancement drops significantly together with the conversion efficiency. To overcome this shortcoming, we explore nonetched L-shaped dielectric nanocylinders and etched arrow-shaped nanoresonators that locally support multiple overlapped resonances maximizing the conversion efficiency. In particular, we show the realistic possibility to achieve up to 4.5% efficiency for a normal incident pump intensity of 50 kW/cm^2, stemming from inherently local phenomena, including saturation effects in the MQW. Finally, we present a comparison between pros and cons of each approach. We believe that our study provides new opportunities for designing highly efficient nonlinear responses from metasurfaces (MSs) coupled to MQW and to maximize their impact on technology.

Keywords: metasurface; multiple quantum wells; nonlinear optics.

***Corresponding author: Andrea Alù**, Photonics Initiative, Advanced Science Research Center, City University of New York, New York, NY 10031, USA; Department of Electrical Engineering, City College of The City University of New York, New York, NY 10031, USA; and Physics Program, Graduate Center, City University of New York, New York, NY 10016, USA, E-mail: aalu@gc.cuny.edu. https://orcid.org/0000-0002-4297-5274

Ahmed Mekawy, Photonics Initiative, Advanced Science Research Center, City University of New York, New York, NY 10031, USA; and Department of Electrical Engineering, City College of The City University of New York, New York, NY 10031, USA

1 Introduction

The quest for novel applications in the midinfrared spectral range is rapidly increasing, drawing a lot of attention in recent years. This spectral range is of particular interest for chemical sensing, since the natural absorption lines of various gases and liquids lie in this region [1, 2]. Moreover, atmospheric transmission windows lie within this same frequency range, offering interesting opportunities for enhanced data transmission and a door for outer space communications [3]. Recently, there have been significant interest in exploring midinfrared metasurfaces for different functionalities, like far-field engineering [4, 5] and thermal emission control [6, 7]. Of particular interest in some of these implementations has been the integration of suitably engineered multiple quantum well (MQW) materials with tailored intersubband (ISB) midinfrared transitions efficiently coupled to photons through electromagnetic engineering of metasurfaces, leading to strong polaritonic responses over an ultrathin platform. These surfaces support strongly nonlinear phenomena, ideal for frequency conversion and generation, and addressing the important need for midinfrared sources with broad tunability operating at room temperature, necessary to explore the applications mentioned above [8].

MQWs have been shown to possess high intrinsic nonlinear susceptibility associated with their ISB transitions, several orders of magnitude larger than conventional nonlinear crystals [9–12]. However, the electronic ISB nonlinearity can be excited only by electric fields polarized normal to the MQW barriers [9], which shows the necessity for an intermediate stage whose main function is to tailor the fields of a normal incident pump to the desired direction to leverage this large nonlinearity. Ultrathin metasurfaces (MSs) made of subwavelength plasmonic inclusions have been shown to provide an ideal bridge between the normal incident pump and the ISB dipole moment in two ways. The MSs can be fabricated on the top of the MQW thin layer, and not only they provide polarization conversion but also they can be designed to support multiply-resonant fields at the pump frequency and the desired converted frequencies, enabling large field

enhancement in the MQW that strongly and efficiently excites the nonlinear transitions. Compared to conventional nonlinear processes, here the response is highly localized around each individual resonator, and sufficiently strong to relax the need for phase matching and enable the control of nonlinear processes at the subwavelength scale, a property that is truly unprecedented in nonlinear optics. MSs can be hence designed to control and steer at will the nonlinear wavefront. This approach has led to a plethora of interesting applications in the midinfrared range, including record-high second harmonic generation (SHG) [13–15], difference frequency generation [16], third harmonic generation (THG) [17], and more. Nonlinear wavefront manipulation based on controlling the local phase and amplitude, such as in the case of Pancharatnam–Berry MSs coupled to MQW has been also shown for wave steering and focusing [18], and for spin-controlled wave mixing [19].

It should be notes that plasmonic MSs on their own can contribute to enhanced nonlinear processes, due to their intrinsic nonlinear response [20]. However, plasmonic nanoparticles showcase a strong nonlinearity at higher frequencies than the midinfrared range of interest for MQW materials, typically around the frequency range where plasmonic resonances arise [21]. At these frequencies, the field enhancement can reach significant values [22], and many nonlinear applications can be explored, including frequency conversion [23–25]. In general specifically tailored plasmonic inclusions can be considered for different nonlinear applications, for example, split-ring resonators have been studied for SHG because they are not centrosymmetric [26, 27], while dolmen-type structures have been used for THG as they provide high field enhancement with narrow spectral linewidth [28]. In addition, due to the ability of controlling the phase response of the frequency converted wave, a single inclusion can be geometrically tuned for more involved nonlinear applications beyond just frequency conversion, for instance for nonlinear wavefront manipulation. Twisted nanodimer antennas have been used for nonlinear chiral imaging [29], and dipole nanoantennas loaded with nonlinear materials for phase conjugation in reflection and transmission modes [30]. Moreover, MSs based on more complex plasmonic inclusions, such as nano-Kirigami inclusions, were explored for unitary optical circular dichroism of SH conversion [31], V-antennas for nonlinear holography with dual polarizations [32], and star-like antennas for nonlinear optical image encoding [33]. In the following, we also use metallic inclusions loaded by MQWs, but we stress that here the MQW substrate provides the core nonlinear response, while the metallic antennas are used to engineer the optical response, enhance the fields and control the polarization, amplitude and phase of the nonlinearly generated light for different nonlinear applications.

While there have been various approaches to MQW polaritonic metasurfaces, based on T-shaped, gamma-shaped, V-shaped and split-ring resonators [14–19, 34], the optimal approach to achieve the largest generation efficiency remains elusive. This work is an attempt to present and compare a few approaches to polaritonic MS designs leveraging MQWs to achieve large SHG. We propose four different MS designs that we believe span the available design space for SHG. They consist of surface lattice resonances (SLRs) [35], embedded eigenstates [36], nonetched and etched plasmonic resonators supporting two overlapped modes at pump and SH frequency, and dielectric resonators.

2 Discussion

A typical SHG metasurface operating in reflection mode, as considered in the rest of this work, is shown in Figure 1a. The nonlinear semiconductor heterostructure is made of repetitions of MQW layers [11] of total thickness h_{MQW}, as shown in the figure. We aim to synthesize a subwavelength MS unit cell (cartoon shown in the inset) that maximizes the second harnmonic generation (SHG) conversion efficiency. Such inclusion, integrated with the MQW and the back-metal reflector, forms our basic "nanocavity" element. We aim at coupling the electronic ISB transitions in MQWs, defined by the conduction band diagram (see inset) with the electromagnetic resonances provided by the nanocavity to maximize the nonlinear response of the system.

SHG is a nonlinear conversion process achieved when an impinging pump beam at wavelength (frequency) 2λ (ω) excites strong normalized electric fields $\zeta_z^{(\omega)}$ inside the MQW cavity polarized in the z direction. When the nanocavity resonance matches the ISB energy, the MQW layers trigger an ISB transition [9, 11] between two quantized energy levels in the conduction band of the quantum wells, as shown in the inset. This transition induces nonlinear polarization currents that oscillate at 2ω, generating normalized fields $\zeta_z^{(2\omega)}$ radiating with wavelength λ. The efficiency of the radiated SH depends on the spatial field overlap at the pump and SH wavelengths, given by

$$\eta = \frac{\omega^2 h_{\mathrm{MQW}}^2}{2\epsilon_0 c_0^3}\left|\chi_{\mathrm{eff}}^{(2)}\right|^2 I_{\mathrm{inc}}\,; \quad \chi_{\mathrm{eff}}^{(2)} = \frac{1}{V_{\mathrm{MQW}}}\int_{V_{\mathrm{MQW}}} \chi_{zzz}^{(2)}(I_z)\zeta_{\omega,z}^2\zeta_{2\omega,z}\,dV \tag{1}$$

where V_{MQW} is the MQW volume, h_{MQW} is the MQW height, c_0 is the speed of light, $\zeta_{i,z}$ is the normalized local field at

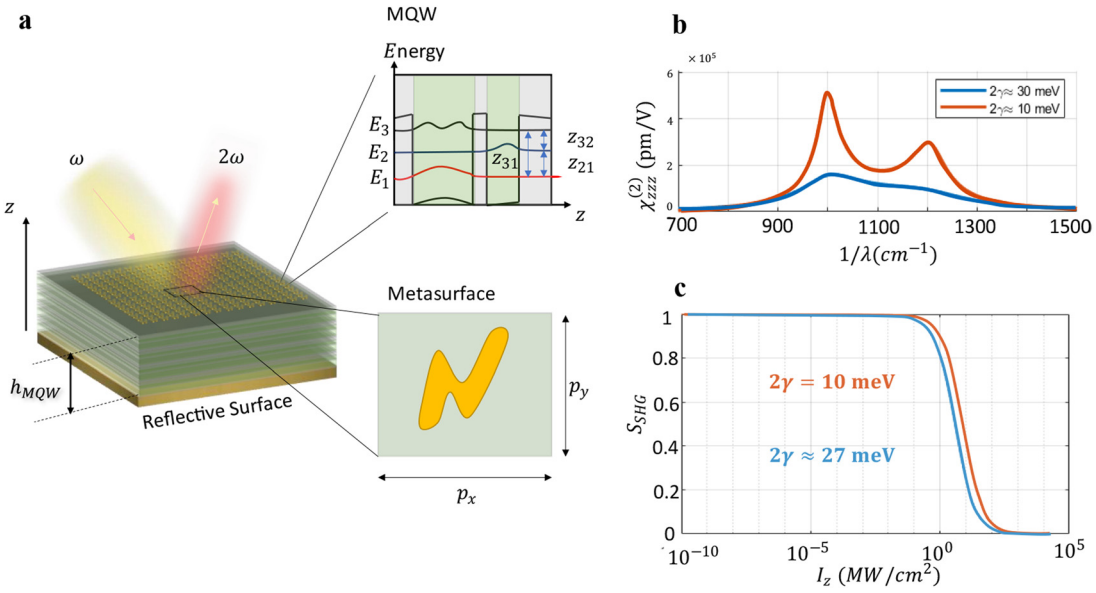

Figure 1: Multiple quantum wells (MQW)-loaded metasurface for second harmonic generation (SHG).
(a) 3D view of the MQW integrated with a metasurface and backed by a metallic reflector for second-harmonic generation in reflection mode. The top panel inset shows the band diagram of the MQW. The bottom panel shows one unit-cell of the metasurface. (b) Nonlinear susceptibility $\chi^{(2)}_{zzz}$ for the bare MQW, and (c) saturation factor S_{SHG} *for* MQW parameters E_{21} = 150 meV, E_{31} = 248 meV, z_{12} = −1.6 nm, z_{23} = −2.3 nm, and z_{13} = −97 nm for $2\gamma_{12,13,23}$ = 10, and 27 meV.

frequency i polarized along z, $\chi^{(2)}_{zzz}$ is the intrinsic tensorial component of the nonlinear susceptibility of the MQW.

Inspecting Eq. (1), we find two main sets of parameters that can control the SHG efficiency. One set corresponds to the MQW material design, identified through the nonlinear susceptibility $\chi^{(2)}_{zzz}$, which can be controlled through material quantum engineering. The second set of parameters that can maximize the nonlinear response is given by the nanocavity geometrical and electromagnetic parameters, which can be aimed at maximizing the overlap integral (1). We start by examining the MQW design parameters that can be optimized for improved SHG efficiency.

2.1 MQW parameters for high SHG efficiency

The nonlinear susceptibility tensor element for SHG at pump frequencies close to the ISB resonances may be approximately written as:

$$\chi^{(2)}_{zzz} = S_{\mathrm{SHG}}(I_z)\frac{N_e e^3}{\hbar^2 \epsilon_0}\frac{z_{12}z_{23}z_{31}}{(E_{31}-2E-i\gamma_{31})(E_{21}-E-i\gamma_{21})} \quad (2)$$

where $S_{\mathrm{SHG}}(I_z)$ is the factor that accounts for saturation effects in the MQW, I_z is the intensity normal to the MQW barriers, N_e is the average bulk doping density, $\hbar\omega_{ij}, 2\hbar\gamma_{ij}$ and ez_{ij} are the energy, linewidth and dipole moment, respectively. Saturation in MQWs occurs when the input intensity is so large that the ISB absorption empties the quantum well ground state of energy E_1 [38, 39]. While this effect can be beneficial for other applications involving limiters [40] or ultrafast optical switches [41], it is the limiting factor for the overall nonlinear frequency conversion achievable with this approach. Equation (1) indeed shows that the SHG efficiency scales with the input power, hence as we increase the incident power we would expect increasing conversion efficiency. However, as we crank up the power, saturation effects emerge, and the efficiency starts to decrease. Therefore, there is an optimal intensity for each metasurface design that guarantees maximum efficiency. Saturation effects in MQWs for ultrathin MS can be predicted analytically [34], and the aim of this paper is to design optimal MS, after considering saturation effects, that achieve maximum generation efficiency complaint with practical available midinfrared laser power levels (50–100 kW/cm^2).

Equation (1) shows that, in addition to designing an MS that maximizes the overlap integral, the intrinsic nonlinear susceptibility of the MQW $\chi^{(2)}_{zzz}$ can be increased by narrowing the linewidth. While the transition energies may be fixed given a spectral window of interest, the ISB linewidth is a prominent factor in determining the nonlinear response. For instance, Figure 1b shows the nonlinear susceptibility for two different linewidths keeping the other parameters constants. We find that it reaches 200 nm/V for

linewidths of 30 meV and is scaled up by five times when the resonance linewidth is 10 meV. Another important feature of reducing the linewidth of ISB transitions is the corresponding relaxation of saturation effects, defined in the factor $S_{\mathrm{SHG}}(I)$. Figure 1c plots the saturation factor $S_{\mathrm{SHG}}(I)$ as a function of input intensity. The turning point for the narrow linewidth is 10 MW/cm^2 while it is only 5 MW/cm^2 for 30 meV linewidth. This implies that the saturation will kick in faster in case of a wider linewidth, thereby limiting the overall efficiency. We conclude that it is better to work with smaller linewidths of the ISB transitions, and correspondingly sharper material resonances.

For SHG applications of MQWs, it was believed that the ideal scenario for the most efficient SHG was given by the condition that the 1–2 transition energy E_{12} equals to the 2–3 transition energy E_{23}, referred to as doubly resonant MQW. Such transition corresponds to a permittivity dispersion following a Drude–Lorentzian model with large imaginary part at the transition energy, which increases the losses at the pump [13] and causes faster saturation. It was recently shown, however, that, different from the doubly resonant MQW designs ($E_{21} = E_{32} = E_{31}/2$) used in MQW-based MSs [7, 13], enhanced efficiency can be achieved if the transition energy between states 1 and 2 is purposefully detuned from the optimal pump energy to reduce optical losses in the nanoresonator cavity and delay saturation effects. In this work, we employ MQWs with engineered transition parameters slightly detuned from the pump photon energy to avoid quick saturation and achieve better conversion efficiency.

2.2 Metasurface parameters for high SHG efficiency

Building on previous explorations for MQW parameters that improve SHG efficiency according to (1), there are still several unexplored venues for the MS design that may enhance the efficiency in (1). While a simple inspection of (1) indicates that the MS design should support large field intensity enhancement, recent attempts have been focused on two enhancement strategies: nanoparticle arrays associated with narrow resonances and high-quality factors (Q-factors), for instance, supporting SLRs [37, 42, 43]; multiply-resonant nanostructures for which the resonance enhancement occurs both at pump wavelength and at the SH wavelength [13–15]. However, it is important to realize that high field enhancements at both frequencies will not necessarily result in improved efficiency. For instance, very high field intensities at the pump frequency can cause saturation to kick in sooner degrading the efficiency significantly. It may be preferable to ensure uniform field distributions across the nanocavity to maximize the use of the MQW nonlinearity. If we then resort of maximizing the field enhancement at the SH frequency, saturation phenomena will be less relevant. This is a particularly successful approach for dielectric MSs, as discussed in Section 3.3.

Hence, we will target an MS that supports high field enhancement at 2ω, which can be achieved by tailoring high Q resonances at this frequency, and moderate field enhancement at the pump frequency, which can be easily achieved using localized resonances. We also explore strong light-matter coupling to maximize the field enhancement. This arises when the rate of interaction between the photonic mode inside the MQW cavity and the transition dipole (electronic mode) is faster than the dissipation rate. Therefore, it requires narrow linewidths of the ISB transitions, and it results in high field intensity enhancement [44, 45]. The spatial distribution of these resonances should still be engineered so that the integral in (1) is maximized, i.e., there should be good overlap between the resonant fields at ω and at 2ω.

3 Results and discussion

We explore in this section different MS designs, and characterize their nonlinear response using full-wave simulations. To model the MQW parameters, the ISTs are characterized by an anisotropic Lorentzian oscillator model, whose dielectric tensor is given by $\epsilon = \epsilon_t(\hat{\mathbf{x}}\hat{\mathbf{x}} + \hat{\mathbf{y}}\hat{\mathbf{y}}) + \epsilon_z\hat{\mathbf{z}}\hat{\mathbf{z}}$, where $\epsilon_t \approx 10.24$ and

$$\epsilon_z = \epsilon_t + \frac{N_e e^2}{\epsilon_0 \hbar}\left(\frac{z_{12}^2}{E_{21} - E - i\gamma_{21}} + \frac{z_{13}^2}{E_{31} - E - i\gamma_{31}}\right) \tag{3}$$

Similarly, in our plasmonic designs, gold is used as the material of choice, and its permittivity is taken from experimental data by Olmon [46]. We provide the details on our full-wave simulations, including how we consider saturation effects, in Section 5.

3.1 Surface lattice resonance

As a first example of high Q resonances for MQW metasurfaces, we explore the use of SLRs. They are collective resonances that arise when individual nanostructures couple to in-plane diffraction orders [47, 48]. The most basic SLR arises when the MS periodicity equals the wavelength at the cutoff of the ±1st diffraction orders, forming standing waves whose quality factor depends on the localized surface plasmon resonance (LSPR) of the inclusion [43, 49]. SLRs are typically characterized by high Q

factors, and they have been explored to enhance the weak nonlinear optical responses of conventional MS [43]. The inclusions themselves can support any kind of additional resonance, as desired, which is particularly useful to enhance the overlap integral between fundamental frequency and SH. Here we explore the role of SLRs in enhancing the nonlinear conversion efficiency in MQW MSs by comparing the SHG efficiency between a conventional MS supporting localized resonances at the two frequencies, and one in which we space the same nanocavities by one wavelength at the second-harmonic frequency to sustain an SLR.

In particular, we consider an etched L-shaped nanocavity as the unit cell of our MS, as shown in Figure 2a, top panel, with the MQW sandwiched between a gold reflector and a 50 nm top gold nanoantenna. This geometry was optimized to support a resonance at the SH wavelength $\lambda = 4$ μm and one at the pump wavelength $2\lambda = 8$ μm, as shown in the absorption spectra in the bottom panel. These simulations are assuming a densely populated array, in which the unit cell periods are much smaller than the generated wavelength, as indicated in the figure. We calculated the mode overlap in the integrand of (1) in the middle panel, showing that the nonlinear polarization currents responsible for nonlinear radiation are localized in a small area near the edges of the nanoantenna.

We now modify the dimensions and the period of the nanocavities, as shown in Figure 2b, such that it support an additional SLR with high Q at λ and another resonance with moderate Q at 2λ. This is achieved by simply making the structure in Figure 2a less dense. Since the nanocavities support a localized resonance at 4 μm, the resonances of the individual nanocavities strongly couple with the lattice resonance resulting in a narrower resonance at 5 μm, and a high $Q \approx 100$ SLR at $\lambda = 4$ μm, as shown in the absorption spectra in the bottom panel. The high Q resonance at λ has two advantages: the spatial distribution of this resonance is a standing wave, as shown in Figure 2b top panel, and this leads to a good mode overlap that extends over a larger area, as shown in the middle panel, when compared to the

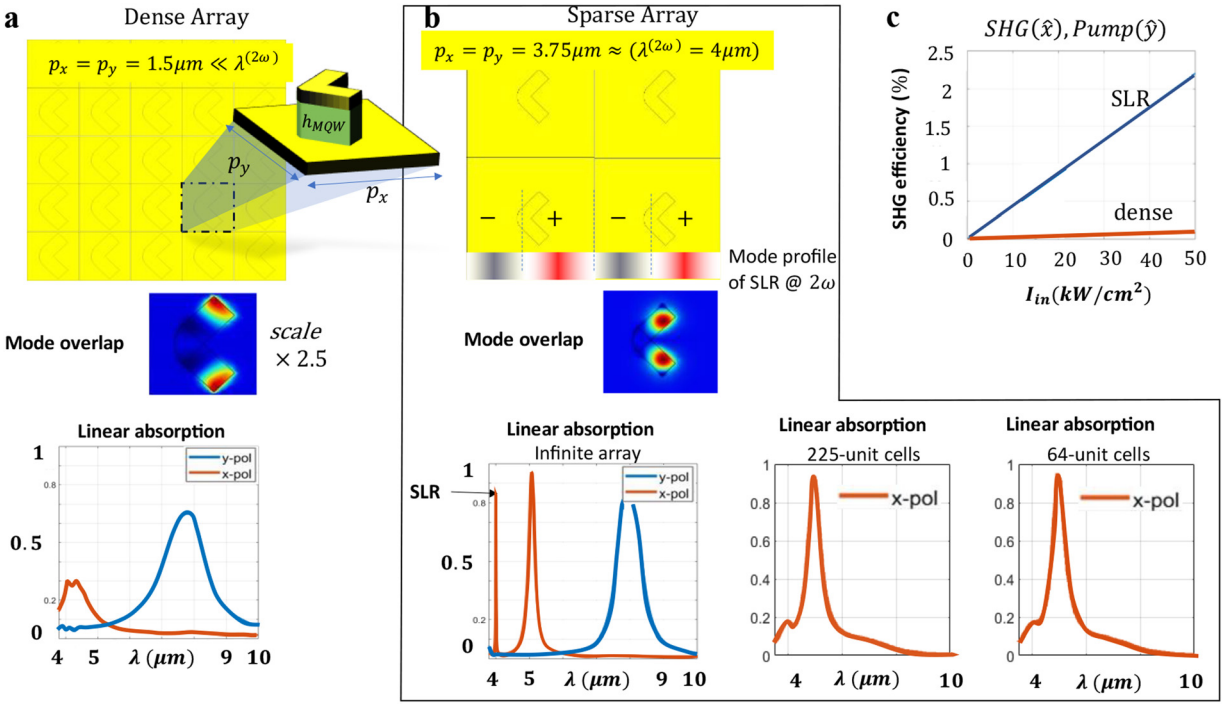

Figure 2: Second harmonic generation (SHG) efficiency from dense metasurfaces supporting a dual resonance, and sparse metasurfaces with additional surface lattice resonance.
(a) Dense array (top panel) supporting dual orthogonal resonances, x-polarized resonance at ω and y-polarized resonance at 2ω (bottom panel), and mode overlap at ω and 2ω at $h_{MQW}/2$ (middle panel). The arm length of the L-shaped nanocavity is 0.6 μm and its width is 0.4 μm, $h_{MQW} = 0.4$ μm, top gold thickness is 50 nm. (b) Sparse array with electric filed distribution at 2ω plotted in the bottom of the figure (top panel) supporting x-polarized resonance at ω, and surface lattice resonance at 2ω for infinite array (bottom panel), and mode overlap between modes at ω and 2ω at $h_{MQW}/2$ (middle panel). The linear absorption for finite array size is shown in the bottom panel for 225 unit cells, and 64 unit cells illuminated. The arm length of the L-shaped nanocavity is 0.755 μm, its width is 0.4 μm, and $h_{MQW} = 0.4$ μm, top gold thickness is 50 nm. (c) $\hat{y}$ polarized second-harmonic generation efficiency for the sparse and dense array at 4 μm and $\hat{x}$-polarized pump at 8 μm with (bottom panel). MQW parameters same as in a.

dense array. In addition, due to its high Q nature, this resonance supports high field intensity enhancement. The drawback is of course that the number of resonators per unit surface is reduced in this second example.

In order to show the difference between the dense and sparse array, we plot the SHG conversion efficiency, neglecting saturation effects for the moment, in Figure 2c for pump wavelength $\lambda = 8$ μm polarized along $\hat{y}$ and SH at $\lambda = 4$ μm polarized along $\hat{x}$ (notice that inversion symmetry is broken for the tensorial vector *xyy*). The conversion efficiency of the sparse array is 26 times larger than the dense array, opening interesting perspectives for nonlinear generation. These results are in line with the results in a study by Czaplicki et al. [37], where it was shown that the two enhancement properties mentioned above, enhanced overlap integral and enhanced fields, improve the nonlinear properties even if at the cost of making the array less dense. As an additional advantage, when saturation phenomena are considered, we expect a reduced sensitivity to saturation in the SLR scenario because of the more spread overlap integral of the resonant fields.

There are however a couple of drawbacks in considering SLR MSs: first, the pump laser power is typically a finite Gaussian beam focused on the surface to enhance the local intensity. Hence, especially for midinfrared excitations, for which power levels are limited, we can expect to illuminate only a finite number of unit cells. For instance, the available data for the pump focal spot on the MSs in similarly coupled plasmonic MQW structure is 35 μm at the laser wavelength of 9 μm [13, 14]. Second, the lattice resonance inherently relies on a collective, highly nonlocal effect, and hence does not allow controlling the nonlinear wavefront at will as in the case of localized resonances, for instance using the approach introduced in [18].

We study the effect of truncating the number of unit cells in the array on the SLR quality factor in Figure 2b bottom panel, which shows the linear absorption for infinite arrays, 225 unit cells and 64 unit cells, therefore we effectively expect a focal spot illumination with diameter of 56 and 30 μm, respectively. These values of the pump illumination beam focal spot are close to the reported values used in experiments [13, 14]. The high-Q resonance of the infinite array rapidly fades away as we decrease the number of unit cells illuminated in the array. We believe this is a fundamental limiting factor for SLR MS in our applications. The typical experiments reported by our group and others for MQW MSs have been typically excited by focused beams with significantly smaller regions than those required to observe the advantages of an SLR.

To overcome this shortcoming, we consider next MS designs based on localized resonances at λ and at 2λ. In order to enhance the local density of states and hence the nonlinear response, we consider engineered MQW responses with ISB transitions with a linewidth of 10 meV, in line with recent experimental realizations of high-quality MQWs [44, 50]. In these designs, we target SHG in the wavelength range $\lambda \approx 5.65$–5.9 μm and consequently pump wavelength range $2\lambda \approx 11.3$–11.8 μm.

3.2 Nonetched L-shaped nanocavities

The development of MQW-loaded MSs for nonlinear harmonic generation has gone through several stages. The first examples were based on nonetched designs, as in [13], in order to maximize the nonlinear material within the substrate of the metasurface. In later stages, etched designs were considered [14–19], noticing that the reduced material volume was largely compensated by enhanced field confinement and overlapped resonances. The nonetched designs typically rely on metallic nanoantennas patterned on the top of an MQW layer, as in the geometry of Figure 2b, while the etched designs consider patterning also the MQW substrate to take the same shape as the nanoantenna. While nonetched designs are easy to fabricate, they have limited field enhancement. For example, the SHG conversion efficiency was 2×10^{-6}% in [13] for nonetched designs, but in subsequent optimized etched designs using the same MQW linewidths the measured efficiency increased to 0.075% [14]. This difference is rooted in the fact that nonetched designs support a mode volume larger than etched ones. This leads to reduced filed intensity close to the nanoantennas, where most of the nonlinear generation occurs. In addition, as mentioned above, the mode overlap is smaller.

Consider for instance an L-shape unetched MS, as shown in the inset of Figure 3a. The structure is optimized to support plasmonic resonances at $2\lambda = 11.61$ μm and at $\lambda = 5.8$ μm for an MQW with ISB at 5.9 μm as shown in the linear absorption in Figure 3a. The mode splitting at 5.9 μm (the ISB wavelength is denoted by red dots) is a clear signature of strong polaritonic coupling between the plasmonic mode and the ISB, and hence high field intensity enhancement. We calculate the conversion efficiency for this structure, considering also saturation effects in the MQW, for pump wavelength $\lambda = 11.8$ μm polarized along $\hat{x}$ and SH at $\lambda = 5.9$ μm polarized also along $\hat{x}$ (notice that inversion symmetry is broken for the tensorial vector *xxx*), as shown in Figure 3b. The conversion efficiency is 0.6% at pump power 20 kW/cm^2, much larger than the one reported in a study by Lee et al. [14] because of the improved design and the sharper transition linewidth of 10 meV.

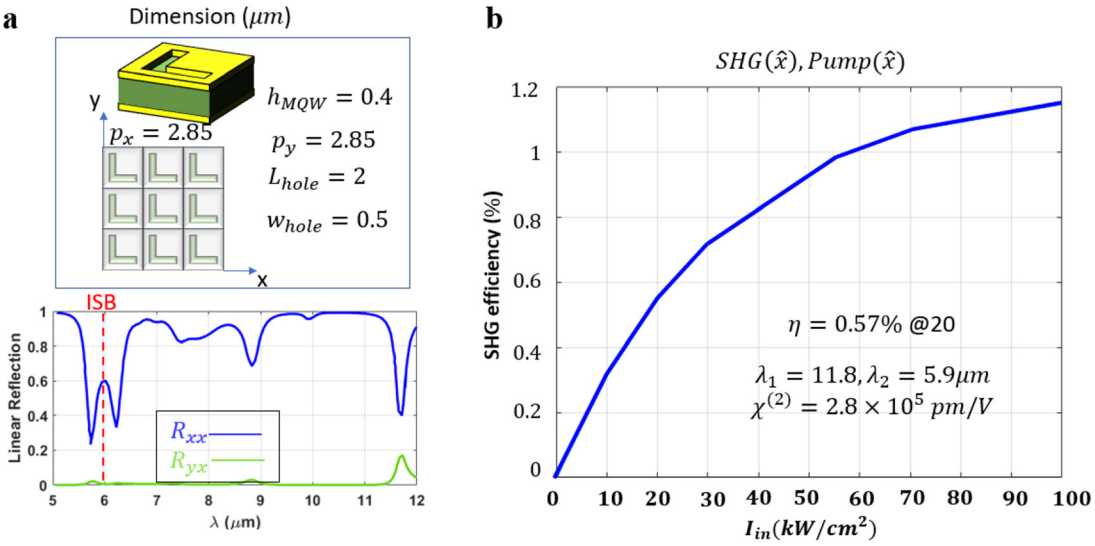

Figure 3: Second harmonic generation (SHG) efficiency for nonetched plasmonic metasurface.
(a) Linear copolymerization and crosspolarization reflection for an *x*-polarized input wave. The inset shows a 3D view of one unit cell, and 2D view of the metasurface looking top down with dimensions in μm. (b) SHG efficiency for $\hat{x}$-polarized pump wavelength 11.8 μm and $\hat{x}$-polarized second-harmonic wavelength 5.9 μm for the metasurface in (a) with inset showing the multiple quantum well (MQW) parameter, and the efficiency at 20 kW/cm^2. MQW parameters are $E_{13} = 207.8$ meV, $E_{21} = 157.3$ meV, $2\gamma = 10$ meV, $z_{12} = -1.76$ nm, $z_{23} = -4.37$ nm and $z_{13} = -1.22$ nm.

3.3 Etched MQWs without metallic nanoantennas

Recently, all-dielectric MSs have emerged as a promising platform to realize exotic light-matter interactions avoiding the inevitable Ohmic losses in metals. As an additional advantage, all-dielectric structures can stand higher power intensities before their breakdown compared to the melting of metallic nanostructures [51]. MQWs are particularly well suited in this regard, since they naturally support a large index of refraction, ideal for field confinement without metal based on Mie resonances. We explore here the possibility of SHG from an all-dielectric MQW metasurface obtained by etching the substrate but avoiding the metallic nanoantenna on top of each etched region. The resulting optimized nanocavity is shown in the inset of Figure 4a. The geometry is optimized to support resonances at fundamental and second-harmonic frequency, and enhancement of the *z*-polarized field in the MQW volume.

We study the response of these all-dielectric metasurfaces in two scenarios. First, we design the structure to support resonances at λ and 2λ. Second, we slightly detune the resonance at 2λ (the dimensions for this geometry are shown in the inset). In general, the MQW is modeled as an anisotropic dielectric, as given by Eq. (3). The dimensions are optimized to give the desired resonance at λ and 2λ. To easily quantify the resonances of such a material we first assume that there is no ISB transition, i.e., $N_e = 0$ in Eq. (3). In this case, the MQW becomes a uniaxial lossless material with refractive index $n_e \approx n_o \approx n_{\mathrm{MQW}} = 3.2$. From there we can easily choose the dimensions of a disk that support a dielectric Mie resonance at the desired frequency. Once we chose the geometry, we introduce in the model the ISB transition in Eq. (3) and perform full-wave simulations. After optimizing the structure dimension, we see that the first geometry leads to larger field enhancement at the pump wavelength 2λ, as expected (see inset of Figure 4b, for the field enhancement for the first geometry on the right, and for the second design on the left). The linear absorption for the detuned geometry is shown in Figure 4a, and it can be readily seen that, due to the broken symmetry of the dielectric, it supports many resonances that can be accessed by a normally incident wave. The reason for the multiple resonances observed in the spectrum is that we need to integrate two resonances at λ and around 2λ in one dielectric inclusion. Hence, the dimensions will be determined by the larger wavelength and, as a result, there are multiple dielectric modes supported at shorter wavelengths. A clear evidence of the supported resonance at $\lambda = 6$ μm is provided by the Rabi splitting associated with the strong polaritonic coupling of electromagnetic and material resonances (the ISB wavelength is denoted by red dots). In addition, it shows a detuned resonance at 10.5 μm. In Figure 4b, we plot the SHG conversion efficiency for this geometry for pump wavelength $\lambda = 11.61$ μm polarized in the direction $\hat{r} = 1/\sqrt{2}\,(\hat{y} + \hat{x})$ and SH at $\lambda = 5.8$ μm polarized in the $\hat{x}$ direction (notice that inversion symmetry is also here broken for the tensorial vector *xrr*), and we compare the result with the case in which the fundamental resonance is tuned with the pump, leading to higher field

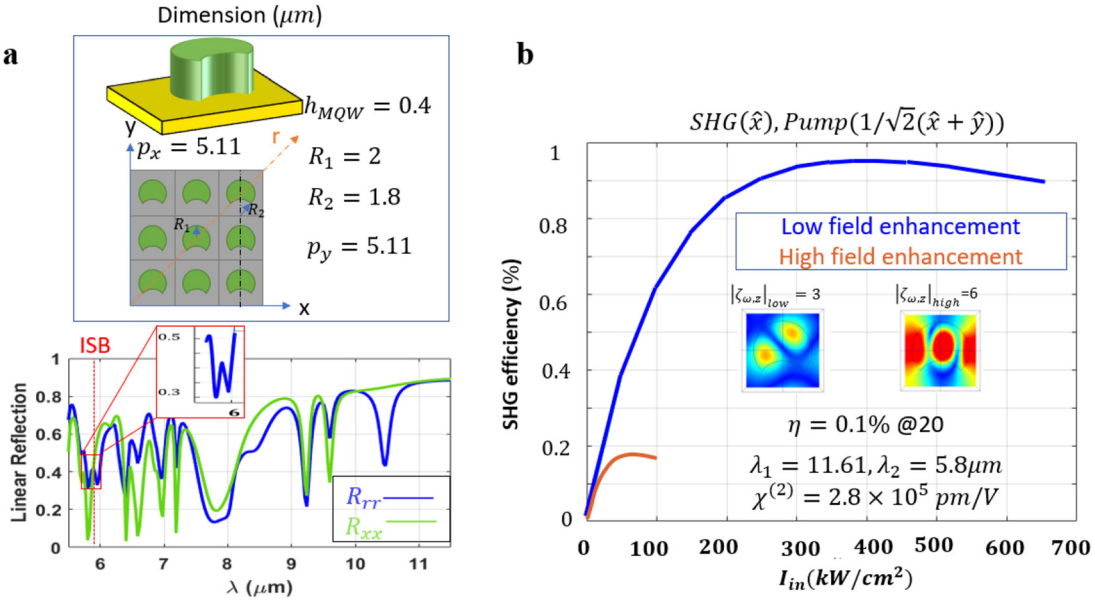

Figure 4: Second harmonic generation (SHG) efficiency for dielectric metasurface.
(a) Linear copolarized reflection for *x*-polarized, and *r*-polarized input wave. The *r* vector is drawn in the inset such that, $\sqrt{2}\hat{r} = \hat{x} - \hat{y}$. The inset shows a 3D view of one-unit cell, and 2D view of the metasurface looking top down with dimensions in μm. (b) SHG efficiency for $\hat{r}$-polarized pump with wavelength 11.61 μm and $\hat{x}$-polarized second harmonic with wavelength 5.8 μm for the metasurface in (a); the inset shows the field enhancement at the pump wavelength for the detuned and tuned designs at the pump wavelength. The efficiency at 20 kW/cm^2 is 0.1%. The multiple quantum well (MQW) parameters are the same as in Figure 3.

enhancement. It is clear that the detuned MS offers much more resilience to saturation effects, due to the lower field profile, enhancing the achievable level of SHG efficiency. Moreover, the dielectric inclusion achieves high efficiency at much larger power compared to the metallic MS considered in Figure 3. For example, the detuned MS achieves a 0.6% SHG efficiency at a pump power of 100 kW/cm^2, compared to only 20 kW/cm^2 for the nonetched MS in Figure 3. While it is true that dielectric MS have lower loss compared to those considering metallic inclusions, it should be noted that the dimensions of the dielectric MS compared to the metallic ones are much larger because of the larger size of the nanoantennas to support Mie resonances. For this reason, both the lateral size and the height of each MQW nanocavity is significantly larger than the metallic MS, limiting the field confinement, overlap integrals and also making more challenging the fabrication.

3.4 Etched arrow-shape MS

To better improve the SHG efficiency, we finally explored etched nanocavities with metallic nanoantennas. We found optimal geometries with an arrow shape, as shown in the inset of Figure 5a. This nanoantenna is somewhat similar to the T-shaped nanoantenna considered in a study by Lee et al. [14], but with tilted arms, and added small vertical arm that improves the spatial overlap integral. Figure 5b shows the calculated efficiency of this design, for pump polarized in the $\hat{x}$ direction at wavelength $2\lambda = 11.3$ μm and SH polarized to the $\hat{y}$ direction at wavelength $\lambda = 5.65$ μm. The SHG efficiency is 3% at 20 kW/cm^2, which we believe represents the best theoretical value for efficiency reported so far for these MQW material parameters. We stress that we have been considering the same material features and linewidth in the calculations in Figures 3–5, showing that the etched substrates capped by metallic nanoantennas appear to provide the ideal response for nonlinear SHG. Field confinement and overlap integral are maximized in these designs, and open to the possibility of achieving close to 5% at moderate input intensities and in a deeply subwavelength volume relying on purely local phenomena, hence ideally suited for nonlinear wavefront shaping and nonlinear metasurface manipulation.

4 Conclusions

In summary, we have presented here a comprehensive overview of the available opportunities in the context of midinfrared metasurface design for SHG. We have shown that SLR approaches can provide very large conversion efficiency, even when large ISB linewidths are considered, but

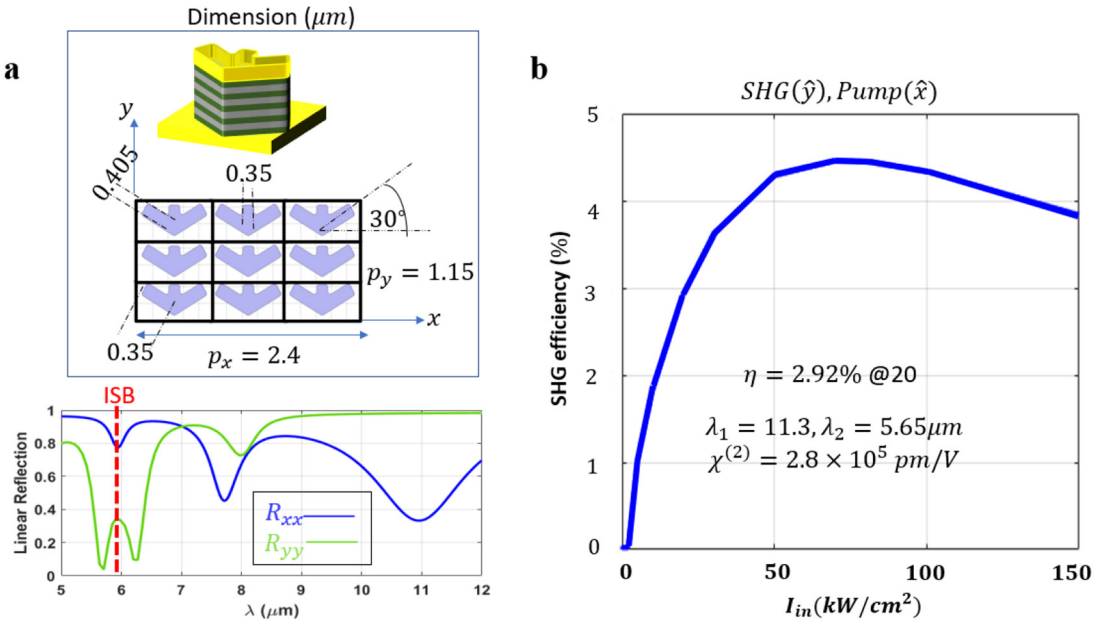

Figure 5: Second harmonic generation (SHG) efficiency for etched metallic metasurface.
(a) Linear copolarized reflection for *x*-polarized and *y*-polarized input waves. The inset shows a 3D view of one unit cell, and 2D view of the metasurface looking top down with dimensions in μm. (b) SHG efficiency for $\hat{x}$-polarized multiple quantum well (MQW) pump wavelength 11.3 μm and $\hat{y}$-polarized second harmonic at 5.65 μm for the metasurface in (a) with the inset showing the MQW parameters, and the efficiency at 20 kW/cm^2. MQW parameters are the same as in Figure 3.

only provided that we can excite the structures uniformly over many unit cells. These requirements prevent the use of this technique for nonlinear metasurface designs. Alternatively, we have explored a few other MS designs based on local overlapped resonances, including non-etched, etched and all-dielectric designs. Our results show the realistic possibility of achieving close to 5% efficiencies with modest pump powers, with the most promising approach relying on etched metallic metasurfaces.

Table 1 summarizes the various approaches described in this paper and their pros and cons. We envision a promising future for midinfrared nonlinear metasurfaces based on MQWs, as we improve the growth and design of these materials and their transition properties, and at the same time we optimize the fabrication and design of the resulting

Table 1: Comparison between different MSs presented in this work and their pros and cons.

Design	η@15 kW/cm^2	Advantages	Challenges
Surface lattice resonance $2\gamma = 30$ meV	0.5%	Large η even with larger ISB linewidth $2\gamma = 27$ meV. High efficiency at low pump power.	Requires very large uniform illumination, as it relies to a highly nonlocal resonance. It does not allow local manipulation of the nonlinear wavefront.
Dielectric inclusions on gold substrate. (ISB linewidth $2\gamma = 10$ meV)	0.05%	It does not require cooling. No metal oxidation or damage. Lower loss, lower heat. Larger saturation thresholds.	Need larger nanoantennas, in the order of $\frac{\lambda}{2}$. It requires high power to reach large efficiencies. Height of MQW is large.
Metallic nonetched designs (ISB linewidth $2\gamma = 10$ meV)	0.3%	Good efficiency even at low power. Small periods $\ll\lambda$. Easy fabrication as the MQW is not patterned.	Requires cooling. Highest efficiency at relatively high power. Metal losses, oxidation, and possible damage at high power levels.
Metallic etched designs (ISB linewidth $2\gamma = 10$ meV)	1.8%	Largest efficiency at low power. Small period $\ll\lambda$. Deeply subwavelength thickness.	Requires cooling. Metal losses, oxidation, and possible damage at high power levels.

ISB, intersubband.

metasurfaces. The reported features open a truly new paradigm for flatland nonlinear optics in the midinfrared region, with applications spanning defense, sensing, thermal manipulation and midinfrared sources.

5 Methods

5.1 Nonlinear simulations including saturation effects

We calculated the SHG efficiency using COMSOL Multiphysics by initially doing two linear frequency domain simulations at ω and at 2ω corresponding to the pump and SH angular frequencies and then doing some post processing over the resulting fields from the linear simulations.

Initially, we assume that all the involved materials are linear, including the MQW, which is modeled using the linear anisotropic permittivity as given in Eq. (3). We perform the simulation for one-unit cell of the MS with periodic boundary conditions excited by a normal incident plane wave with small intensity $I_{\text{inc},0}$ (in simulation we can choose $I_{\text{inc},0}$ such that it is much less than the saturation intensity). This excitation will induce an electric field inside the MQW, with normalized field given as, $\zeta_{\alpha,z}(\mathbf{r}) = \frac{E_{\alpha,z}(\mathbf{r})}{E_0}$, where E_0 is the electric field value of the incident plane wave and $\alpha = \omega$, *or* 2ω is the input frequency.

To calculate the SHG efficiency as defined in Eq. (1), knowing the normalized z field components at ω ($\zeta_{\omega,z}$) and at 2ω ($\zeta_{2\omega,z}$) from the previous step, we perform a spatial integration over the MQW volume as:

$$P(I_{\text{inc},0}) = \int_{\text{MQW}} S_{\text{SHG}}\left(I_z(\mathbf{r}, I_{\text{inc},0})\right)\left(\zeta_{\omega,z}(\mathbf{r})\right)^2 \zeta_{2\omega,z}(\mathbf{r})dv \tag{4}$$

Notice that $S_{\text{SHG}}(I_z(\mathbf{r}, I_{\text{inc},0})) = 1$ since $I_{\text{inc},0} \ll I_{\text{sat}}$, where I_{sat} is the saturation intensity corresponding to the intensity turning point in Figure 1c, and $I_z = 2n_{\text{MQW}}\epsilon_0 c\left|E_{\omega,z}(\mathbf{r}, I_{\text{inc},0})\right|^2$, where $\mathbf{r}$ is the spatial position inside the MQW, and n_{MQW} is the refractive index of the MQW, ϵ_0 is the vacuum permittivity, and c is the speed of light.

We can plug the previous integral value in Eq. (1) to calculate the low power SHG efficiency, i.e., at $I_{\text{inc},0}$. As we increase the incident power to higher value $I_{\text{inc}} > I_{\text{inc},0}$, we do not need to perform further simulations to calculate the saturation effect. Since we assume that the material parameters do not change significantly, this is true for the given MQW structures which have low saturation intensities, therefore increasing the incident power affects only the term $S_{\text{SHG}}(I_z(\mathbf{r}, I_{\text{inc},0}))$ in Eq. (4) which can be written as a function of the saturation factor S_{SHG} at the low incident power $I_{\text{inc},0}$ as,

$$S_{\text{SHG}}(I_z(\mathbf{r}, I_{\text{inc}})) = S\left(I_z(\mathbf{r}, I_{\text{inc},0})I_{\text{inc}}/I_{\text{inc},0}\right)$$

Therefore, we recalculate the spatial integral at all intensities, given as,

$$P(I_{\text{inc}}) = \int_{\text{MQW}} S_{\text{SHG}}\left(I_z(\mathbf{r}, I_{\text{inc},0})I_{\text{inc}}/I_{\text{inc},0}\right)\left(\zeta_{\omega,z}(\mathbf{r})\right)^2 \zeta_{2\omega,z}(\mathbf{r})dv$$

It is readily seen from Eq. (1) that the efficiency η is proportional to the multiplication $P(I_{\text{inc}})\, I_{\text{inc}}$, so there is an optimal power level for the highest efficiency as shown in Figures 3b, 4b, 5b as a result of the competition between two functions, $P(I_{\text{inc}})[I_{\text{inc}}]$ that decreases [increases] with increasing the input intensity.

While this is the method we used to calculate the SHG efficiency in this work, one commonly used method is based on coupled nonlinear simulations. In this case, one performs linear simulations at frequency ω producing a nonlinear polarization current P_{NL}

$$P_{NL,z} = i2\omega_0 S(\mathbf{r}, I_{\text{inc}})\chi^{(2)}_{zzz}E^2_{\omega,z},$$

which will be used as the excitation for a second frequency domain simulation at $2f_0$. We then calculated the radiated power from the MS at 2ω to calculate the SHG efficiency by normalizing that power intensity to the incident power intensity. In general, both approaches provide similar results but the former one has shortest computation time, yet it is valid for very thin metasurfaces $h_{\text{MQW}} \ll \lambda$, and for SH radiation without additional diffraction orders, which is the scenario of interest in this work.

Acknowledgements: This work was supported by the Defense Advanced Research Projects Agency NASCENT program, a Department of Defense Vannevar Bush Faculty Fellowship, and the Air Force Office of Scientific Research MURI program.

Author contribution: All the authors have accepted responsibility for the entire content of this submitted manuscript and approved submission.

Research funding: This work was supported by the Defense Advanced Research Projects Agency NASCENT program, a Department of Defense Vannevar Bush Faculty Fellowship, and the Air Force Office of Scientific Research MURI program.

Conflict of interest statement: The authors declare no conflicts of interest regarding this article.

References

[1] B. Van Eerdenbrugh and L. S. Taylor, "Application of mid-IR spectroscopy for the characterization of pharmaceutical systems," *Int. J. Pharm.*, vol. 417, nos. 1–2, pp. 3–16, 2011.

[2] G. V. Naik, V. M. Shalaev, and A. Boltasseva, "Alternative plasmonic materials: beyond gold and silver," *Adv. Mater.*, vol. 25, no. 24, pp. 3264–3294, 2013.

[3] M. Sieger and B. Mizaikoff, "Toward on-chip mid-infrared sensors," *Anal. Chem.*, vol. 88, no. 11, pp. 5562–5573, 2016.

[4] D. G. Baranov, Y. Xiao, I. A. Nechepurenko, A. Krasnok, A. Alù, and M. A. Kats, "Nanophotonic engineering of far-field thermal emitters," *Nat. Mater.*, vol. 18, pp. 920–930, 2019.

[5] R. Duggan, Y. Ra'di, and A. Alù, "Temporally and spatially coherent emission from thermal embedded eigenstates," *ACS Photonics*, vol. 6, no. 11, pp. 2949–2956, 2019.

[6] M. De Zoysa, T. Asano, K. Mochizuki, A. Oskooi, T. Inoue, and S. Noda, "Conversion of broadband to narrowband thermal emission through energy recycling," *Nat. Photonics*, vol. 6, no. 8, pp. 535–539, 2012.

[7] T. Inoue, M. De Zoysa, T. Asano, and S. Noda, "High-*Q* mid-infrared thermal emitters operating with high power-utilization efficiency," *Opt. Express*, vol. 24, no. 13, pp. 15101–15109, 2016.

[8] J. Faist, F. Capasso, C. Sirtori, et al., "High power mid-infrared ($\lambda \sim 5$ μm) quantum cascade lasers operating above room temperature," *Appl. Phys. Lett.*, vol. 68, no. 26, pp. 3680–3682, 1996.
[9] E. Rosencher, A. Fiore, B. Vinter, V. Berger, P. Bois, and J. Nagle, "Quantum engineering of optical nonlinearities," *Science*, vol. 271, pp. 168–173, 1996.
[10] E. Rosencher, P. Bois, J. Nagle, and S. Delattre, "Second harmonic generation by intersub-band transitions in compositionally asymmetrical MQWs," *Electron. Lett.*, vol. 25, p. 1063, 1989.
[11] F. Capasso, C. Sirtori, and A. Y. Cho, "Coupled quantum well semiconductors with giant electric field tunable nonlinear optical properties in the infrared," *IEEE J. Quantum Electron.*, vol. 30, pp. 1313–1326, 1994.
[12] M. M. Fejer, S. J. B. Yoo, R. L. Byer, A. Harwit, and J. S. Harris Jr., "Observation of extremely large quadratic susceptibility at 9.6–10.8 μm in electric-field-biased AlGaAs quantum wells," *Phys. Rev. Lett.*, vol. 62, pp. 1041–1044, 1989.
[13] J. Lee, M. Tymchenko, C. Argyropoulos, et al., "Giant nonlinear response from plasmonic metasurfaces coupled to intersubband transitions," *Nature*, vol. 511, no. 7507, pp. 65–69, 2014.
[14] J. Lee, N. Nookala, J. S. Gomez-Diaz, et al., "Ultrathin second-harmonic metasurfaces with record-high nonlinear optical response," *Adv. Opt. Mater.*, vol. 4, no. 5, pp. 664–670, 2016.
[15] R. Sarma, D. de Ceglia, N. Nookala, et al., "Broadband and efficient second-harmonic generation from a hybrid dielectric metasurface/semiconductor quantum-well structure," *ACS Photonics*, vol. 6, no. 6, pp. 1458–1465, 2019.
[16] M. Tymchenko, J. S. Gomez-Diaz, J. Lee, M. A. Belkin, and A. Alù, "Highly-efficient THz generation using nonlinear plasmonic metasurfaces," *J. Opt.*, vol. 19, no. 10, p. 104001, 2017.
[17] J. Yu, S. Park, I. Hwang, D. Kim, J. Y. Jung, and J. Lee, "Third-harmonic generation from plasmonic metasurfaces coupled to intersubband transitions," *Adv. Opt. Mater.*, vol. 7, no. 9, p. 1801510, 2019.
[18] M. Tymchenko, J. S. Gomez-Diaz, J. Lee, N. Nookala, M. A. Belkin, and A. Alù, "Gradient nonlinear pancharatnam-berry metasurfaces," *Phys. Rev. Lett.*, vol. 115, no. 20, p. 207403, 2015.
[19] D. Kim, H. Chung, J. Yu, et al., "Spin-controlled nonlinear harmonic generations from plasmonic metasurfaces coupled to intersubband transitions," *Adv. Opt. Mater.*, vol. 8, p. 2000004, 2020.
[20] E. Rahimi and R. Gordon, "Nonlinear plasmonic metasurfaces," *Adv. Opt. Mater.*, vol. 6, no. 18, p. 1800274, 2018.
[21] S. A. Maier, *Plasmonics: Fundamentals and Applications*, New York, NY, Springer Science & Business Media, 2007.
[22] H. Yu, Y. Peng, Y. Yang, and Z. Y. Li, "Plasmon-enhanced light–matter interactions and applications," *NPJ Comput. Mater.*, vol. 5, no. 1, pp. 1–14, 2019.
[23] M. Kauranen and A. V. Zayats, "Nonlinear plasmonics," *Nat. Photonics*, vol. 6, no. 11, pp. 737–748, 2012.
[24] G. Li, S. Chen, N. Pholchai, et al., "Continuous control of the nonlinearity phase for harmonic generations," *Nat. Mater.*, vol. 14, no. 6, pp. 607–612, 2015.
[25] N. C. Panoiu, W. E. I. Sha, D. Y. Lei, and G. C. Li, "Nonlinear optics in plasmonic nanostructures," *J. Opt.*, vol. 20, no. 8, p. 083001, 2018.
[26] C. Ciracì, E. Poutrina, M. Scalora, and D. R. Smith, "Origin of second-harmonic generation enhancement in optical split-ring resonators," *Phys. Rev. B*, vol. 85, no. 20, p. 201403, 2012.
[27] S. Linden, F. B. P. Niesler, J. Förstner, Y. Grynko, T. Meier, and M. Wegener, "Collective effects in second-harmonic generation from split-ring-resonator arrays," *Phys. Rev. Lett.*, vol. 109, no. 1, p. 015502, 2012.
[28] B. Metzger, T. Schumacher, M. Hentschel, M. Lippitz, and H. Giessen, "Third harmonic mechanism in complex plasmonic Fano structures," *ACS Photonics*, vol. 1, no. 6, pp. 471–476, 2014.
[29] M. J. Huttunen, G. Bautista, M. Decker, S. Linden, M. Wegener, and M. Kauranen, "Nonlinear chiral imaging of subwavelength-sized twisted-cross gold nanodimers," *Opt. Mater. Express*, vol. 1, no. 1, pp. 46–56, 2011.
[30] P. Y. Chen and A. Alù, "Subwavelength imaging using phase-conjugating nonlinear nanoantenna arrays," *Nano Lett.*, vol. 11, no. 12, pp. 5514–5518, 2011.
[31] Y. Tang, Z. Liu, J. Deng, K. Li, J. Li, and G. Li, "Nano-Kirigami metasurface with giant nonlinear optical circular dichroism," *Laser Photonics Rev.*, vol. 14, p. 2000085, 2020.
[32] E. Almeida, O. Bitton, and Y. Prior, "Nonlinear metamaterials for holography," *Nat. Commun.*, vol. 7, no. 1, pp. 1–7, 2016.
[33] F. Walter, G. Li, C. Meier, S. Zhang, and T. Zentgraf, "Ultrathin nonlinear metasurface for optical image encoding," *Nano Lett.*, vol. 17, no. 5, pp. 3171–3175, 2017.
[34] J. S. Gomez-Diaz, M. Tymchenko, J. Lee, M. A. Belkin, and A. Alù, "Nonlinear processes in multi-quantum-well plasmonic metasurfaces: electromagnetic response, saturation effects, limits, and potentials," *Phys. Rev. B*, vol. 92, no. 12, p. 125429, 2015.
[35] M. Minkov, D. Gerace, and S. Fan, "Doubly resonant χ (2) nonlinear photonic crystal cavity based on a bound state in the continuum," *Optica*, vol. 6, no. 8, pp. 1039–1045, 2019.
[36] Z. Sakotic, A. Krasnok, N. Cselyuszka, N. Jankovic, and A. Alú, "Berreman embedded eigenstates for narrowband absorption and thermal emission," arXiv preprint arXiv:2003.07897, 2020.
[37] R. Czaplicki, A. Kiviniemi, M. J. Huttunen, et al., "Less is more: enhancement of second-harmonic generation from metasurfaces by reduced nanoparticle density," *Nano Lett.*, vol. 18, no. 12, pp. 7709–7714, 2018.
[38] K. L. Vodopyanov, V. Chazapis, C. C. Phillips, B. Sung, and J. S. Harris Jr., "Intersubband absorption saturation study of narrow III–V multiple quantum wells in the $\lambda = 2.8$–9 μm spectral range," *Semicond. Sci. Technol.*, vol. 12, p. 708, 1997.
[39] R. W. Boyd, *Nonlinear Optics*, 3rd ed., New York, Academic, 2008, p. 640.
[40] H. Qian, S. Li, Y. Li, et al., "Nanoscale optical pulse limiter enabled by refractory metallic quantum wells," *Sci. Adv.*, vol. 6, no. 20, p. eaay3456, 2020.
[41] G. Günter, A.A. Anappara, J. Hees, et al., "Sub-cycle switch-on of ultrastrong light–matter interaction," *Nature*, vol. 458, no. 7235, pp. 178–181, 2009.
[42] M. J. Huttunen, P. Rasekh, R. W. Boyd, and K. Dolgaleva, "Using surface lattice resonances to engineer nonlinear optical processes in metal nanoparticle arrays," *Phys. Rev. A*, vol. 97, no. 5, p. 053817, 2018.
[43] M. J. Huttunen, O. Reshef, T. Stolt, K. Dolgaleva, R. W. Boyd, and M. Kauranen, "Efficient nonlinear metasurfaces by using multiresonant high-*Q* plasmonic arrays," *JOSA B*, vol. 36, no. 7, pp. E30–E35, 2019.
[44] A. Benz, S. Campione, S. Liu, et al., "Strong coupling in the sub-wavelength limit using metamaterial nanocavities," *Nat. Commun.*, vol. 4, no. 1, pp. 1–8, 2013.
[45] O. Wolf, A. A. Allerman, X. Ma, et al., "Enhanced optical nonlinearities in the near-infrared using III-nitride

heterostructures coupled to metamaterials," *Appl. Phys. Lett.*, vol. 107, no. 15, p. 151108, 2015.

[46] R. L. Olmon, B. Slovick, T. W. Johnson, et al., "Optical dielectric function of gold," *Phys. Rev. B*, vol. 86, no. 23, p. 235147, 2012.

[47] V. G. Kravets, A. V. Kabashin, W. L. Barnes, and A. N. Grigorenko, "Plasmonic surface lattice resonances: a review of properties and applications," *Chem. Rev.*, vol. 118, no. 12, pp. 5912–5951, 2018.

[48] D. Khlopin, F. Laux, W. P. Wardley, et al., "Lattice modes and plasmonic linewidth engineering in gold and aluminum nanoparticle arrays," *JOSA B*, vol. 34, no. 3, pp. 691–700, 2017.

[49] M. Saad Bin-Alam, O. Reshef, Y. Mamchur, et al., Ultra-high-*Q* resonances in plasmonic metasurfaces," arXiv preprint arXiv: 2004.05202v1, 2020, https://doi.org/10.1109/pn50013.2020.9167033.

[50] S. Campione, A. Benz, J. F. Klem, M. B. Sinclair, I. Brener, and F. Capolino, "Electrodynamic modeling of strong coupling between a metasurface and intersubband transitions in quantum wells," *Phys. Rev. B*, vol. 89, no. 16, p. 165133, 2014.

[51] P. R. West, S. Ishii, G. V. Naik, N. K. Emani, V. M. Shalaev, and A. Boltasseva, "Searching for better plasmonic materials," *Laser Photonics Rev.*, vol. 4, no. 6, pp. 795–808, 2010.